Measurement of instantaneous velocity and surface topography in the wake of a cylinder at low Reynolds number

A. Fouras[a,b,*], D. Lo Jacono[b], G.J. Sheard[b], K. Hourigan[a,b]

[a]*Division of Biological Engineering, Monash University, 3800 Melbourne, Australia*
[b]*FLAIR, Department of Mechanical and Aerospace Engineering, Monash University, 3800 Melbourne, Australia*

Abstract

A technique capable of simultaneous measurement of free-surface topography and velocity vector field data is presented. This technique offers substantial benefits of both reduced complexity and enhanced accuracy over all other techniques known to offer the same measurements. The flow behind a circular cylinder at low Reynolds numbers is measured using this technique. The velocity and vorticity fields as well as Strouhal number closely match the expected results. The free-surface topography, which can be related to the pressure field, exhibits an intimate relationship to the vorticity field.

© 2008 Elsevier Ltd. All rights reserved.

Keywords: Surface topography; PIV; Pressure-field; Cylinder wake

1. Introduction

A number of fluid mechanics studies could benefit from the simultaneous measurement of both velocity field data (and related quantities such as vorticity) and surface topography. Recent examples of such studies are the study by Fu and Rockwell (2005) of shallow flow around a circular cylinder and the recent study by Buchanan et al. (2007) of supersonic jet screech, using the hydraulic analogy. Typically, the free-surface topography relates to the pressure field through the low Froude number modified equations of motion (Buchanan et al., 2007).

A number of point and area measurement techniques have been developed over recent decades to measure the free-surface topography. The most promising of these techniques are the optical area measurement techniques detailed in Tanaka et al. (2000) and Zhang et al. (1994). These techniques were enhanced by Fouras et al. (2006) with a new technique that is more accurate and simpler to implement.

2. Methodology

The new technique described in this paper is based on an integral combination of particle image velocimetry (PIV) (Raffel et al., 1998) and the reference image topography technique is described in Fouras et al. (2006). In this technique,

*Corresponding author at: Division of Biological Engineering, Monash University, 3800 Melbourne, Australia.
E-mail address: fouras@eng.monash.edu (A. Fouras).

experiments are conducted in a glass bottomed water table. The water is seeded with particles and the horizontal plane (selected as the plane for velocity measurement) is illuminated by a laser sheet. Twin cameras are symmetrically installed on the water table with one above the free surface and one below the glass bottom, as shown in Fig. 1. These cameras are positioned to achieve approximately the same magnification and field of view. Under conditions of a flat water surface, the images from the top camera can be related to the images from the bottom camera by a mapping function which can be evaluated using techniques described by Fouras et al. (2007, 2008).

Fig. 2 describes the process of analysing the data from the top and bottom cameras to yield the velocity and height data. The images acquired through the flat glass bottom can be interrogated to yield the velocity data using PIV analysis. When the images from the top and bottom are compared using PIV analysis (taking into account the mapping function evaluated under flat or still conditions), the resultant apparent displacement field must be the result of refraction of light through the distorted free surface. The displacement field is related to free-surface gradients, which can be integrated to yield the free-surface topography. An algorithm to perform this integration with minimal sensitivity to noise while maintaining fine detail is described in Section 2.1.

2.1. Obtaining surface topography from PIV displacement data

The PIV analysis of the experimental images produces a grid of displacement vectors corresponding to the optical distortion of laser light scattered by the seeding particles due to refraction through the surface of the liquid–air interface. At each point, the components of the displacement vector in Cartesian coordinates are (δ_x, δ_y). The goal of the numerical surface height integration is to obtain the height H at each point, given a reference height H_{ref}. In this paper, a robust technique for obtaining the surface topography in a manner devoid of any positional bias is proposed. It will later be shown that the least-squares integration approach filters random remaining errors from the PIV process, while reproducing fine details in the true free-surface topography.

At each location, the gradient of the surface is $\partial H/\partial \mathbf{x}$ where the spatial coordinate vector $\mathbf{x} = \langle x, y \rangle$. The surface gradient is related to H, δ_x and δ_y by the physics of refraction, as shown in Fig. 3 in one dimension.

Using Snell's law of refraction ($\eta_{\text{air}} \sin \alpha_1 = \eta_{\text{liquid}} \sin \alpha_2$) the relationship

$$\tan^{-1} \frac{\delta_x}{H} = \tan^{-1} \frac{\partial H}{\partial x} - \sin^{-1} \left[\eta_r \sin \left(\tan^{-1} \frac{\partial H}{\partial x} \right) \right] \tag{1}$$

can be derived based on the configuration shown in Fig. 3, where the refractive index ratio $\eta_r = \eta_{\text{air}}/\eta_{\text{liquid}}$ is introduced.

Numerically, the surface gradient $\partial H/\partial x$ can be approximated by some numerical differentiation scheme as $\Delta H/\Delta x$; for example a forward- or centred-difference scheme. The important point is that these schemes are typically represented by local function values (H_i) and point spacings (Δx_i). An appropriate strategy for obtaining the topography solution H is to employ a root-finding method on (1) to determine surface gradient estimates at each point, then to integrate these gradients to find an estimate of the topography, before iteratively repeating this process with improved guesses of H.

The following algorithm is proposed for solving for the heights H, given a reference height H_{ref}, and displacements δ_x and δ_y:

(i) set heights $H = H_{\text{ref}}$;
(ii) use Eq. (1) and the current guesses of H to estimate $\partial H/\partial x$ and $\partial H/\partial y$ at each point;
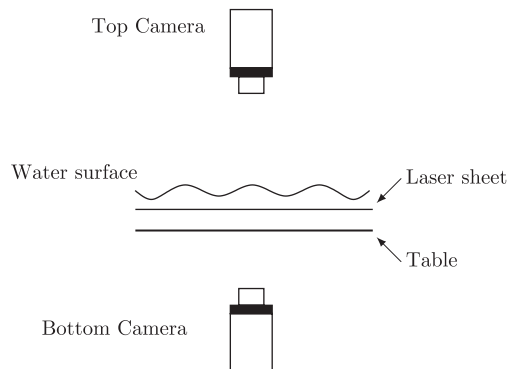

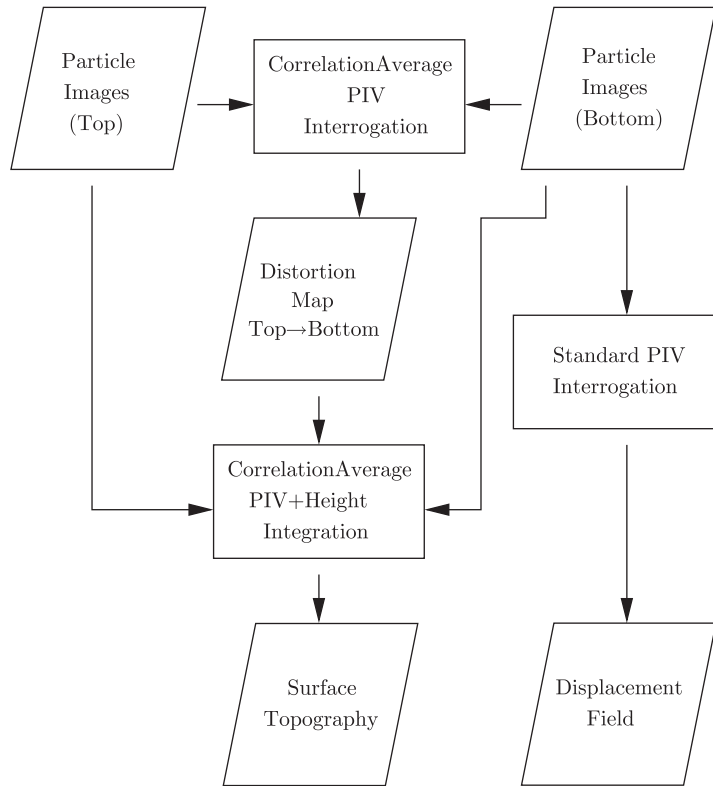Fig. 1. Schematic of the configuration of cameras and light sheet relative to the surface.

Fig. 2. The processing methodology used to calculate both the velocity and topography data.
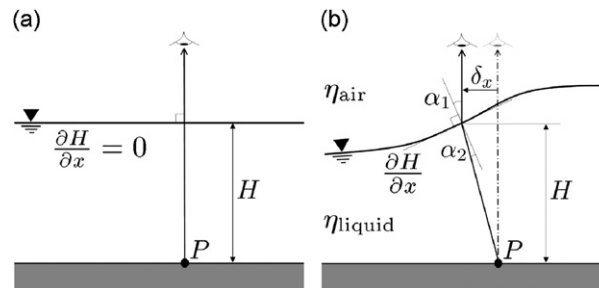

Fig. 3. (a) The undistorted position of a point P (on the laser sheet, shaded grey) viewed from a distant location through an undisturbed free surface. (b) The apparent displacement δ_x of point P due to refraction through the surface at height H with gradient $\partial H/\partial x$. Refractive indices of the air (η_{air}) and liquid (η_{liquid}) phases are shown, as are the refraction angles α_1 and α_2.

(iii) integrate gradients ($\partial H/\partial x$ and $\partial H/\partial y$) to find estimate of heights (H_{est});
(iv) shift H_{est} to minimize the error between measured refraction displacements, and those predicted by numerical ray tracing;
 (v) the adjusted heights H_{adjust} can be refined by repeating steps 2–4 until the difference between successive H_{adjust} values converges.

   The following section describes in detail the procedure used to integrate the gradient data for the surface topography (step 3).

2.2. Integration of surface gradients for surface topography

At each point on the surface, gradients in x and y are known. If the total number of data points is N, then based on numerical estimates of the surface gradients, an over-prescribed matrix system

$$\mathbf{AH} = \mathbf{b}, \tag{2}$$

can be established where $\mathbf{A}$ is a $(2N+1) \times N$ matrix containing numerical derivative estimates in x and y for each point, plus a function of the reference height H_{ref} to maintain the consistency of the matrix, $\mathbf{H}$ is a solution vector of length N representing the surface heights, and $\mathbf{b}$ is a vector of length $2N+1$ containing the gradients obtained from the refraction physics and displacement data. Written in full, this becomes

$$\mathbf{AH} = \begin{bmatrix} \mathbf{D}_x \\ \mathbf{D}_y \\ \mathbf{A}_{\text{ref}} \end{bmatrix} \begin{bmatrix} H_1 \\ \vdots \\ H_N \end{bmatrix} = \mathbf{b} = \begin{bmatrix} \left.\frac{\partial H}{\partial x}\right|_1 \\ \vdots \\ \left.\frac{\partial H}{\partial x}\right|_N \\ \cdots \cdots \\ \left.\frac{\partial H}{\partial y}\right|_1 \\ \vdots \\ \left.\frac{\partial H}{\partial y}\right|_N \\ \cdots \cdots \\ b_{\text{ref}} \end{bmatrix}. \tag{3}$$

As $\mathbf{A}$ is not a square matrix, the solution for $\mathbf{H}$ cannot be obtained by direct inversion of $\mathbf{A}$. Instead, a solution is found in a least-squares sense by obtaining the pseudo-inverse of $\mathbf{A}$, i.e.,

$$\mathbf{H} = (\mathbf{A}^{\text{T}}\mathbf{A})^{-1}\mathbf{A}^{\text{T}}\mathbf{b}. \tag{4}$$

For problems of a practical size, $\mathbf{A}$ quickly becomes too large to store in full. For example, when $N = 50 \times 50$, $\mathbf{A}$ becomes a 5001×2500 matrix. Fortunately, with an appropriate selection of derivative approximation technique, $\mathbf{A}$ is very sparse. For instance, forward or centred difference approximations produce only two non-zero elements per row, with the exception of the final row. The final row of $\mathbf{A}$ specifies an equation relating the unknown heights $\mathbf{H}$ to the reference height H_{ref}. An ideal equation would equate the mean height to the reference height

$$\sum_{i=1}^{N} H_i = NH_{\text{ref}}, \tag{5}$$

but this generates a full row in $\mathbf{A}$, which then renders the matrix product $\mathbf{A}^{\text{T}}\mathbf{A}$ full. A high sparsity of $\mathbf{A}^{\text{T}}\mathbf{A}$ can be maintained, however, if a simpler reference height relationship (e.g., $H_1 = H_{\text{ref}}$) is adopted instead.

In the present implementation, $\mathbf{A}$ and $\mathbf{A}^{\text{T}}\mathbf{A}$ were constructed using the compressed sparse row (CSR) sparse matrix storage format, with derivatives at the edges of the image estimated using forward- and backward-differences, and at interior points using centred-differences. The solution of the linear problem

$$(\mathbf{A}^{\text{T}}\mathbf{A})\mathbf{H} = \mathbf{A}^{\text{T}}\mathbf{b} \tag{6}$$

was obtained using the PARDISO package (Schenk and Gartner, 2004). The symmetry of $\mathbf{A}^{\text{T}}\mathbf{A}$ meant that only the upper-diagonal component needed to be stored, further reducing the strain on storage requirements.

In the present implementation of the surface topography integration technique, the assembly of $\mathbf{A}$, and the assembly and factorization of $\mathbf{A}^{\text{T}}\mathbf{A}$ were completed prior to entering the iterative loop, leaving only a sparse matrix–vector product operation ($\mathbf{A}^{\text{T}}\mathbf{b}$), and a sparse matrix solution to be completed during each iteration.

3. Results

The experiments reported in this paper were performed on a water table shown schematically in Fig. 4. The splitter plate was 25 mm above the table floor. The water height above the splitter plate was about $H_{\text{ref}} = 51$ mm and the

cylinder had diameter $D = 3.9$ mm. Polyamide-based particles (Vestosint) with characteristic diameter of 26 μm are used as seeding tracers for PIV. At each Reynolds number, 200 frame pairs were acquired. The image pair acquisition rate was 5 Hz and the time interval between images within a pair was 20 ms. A Reynolds number is defined as $Re = UD/v$, where U is the velocity of the oncoming flow, D is the cylinder diameter and v the kinematic viscosity. A Strouhal number is defined as $St = fD/U$ where f is the frequency of shedding. For parallel shedding, previous studies [e.g., Williamson (1988a), Williamson and Brown (1998)] propose a linear relationship between the shedding frequency and the inverse square root of the Reynolds number. The vorticity is calculated by a combination of least-squares fitting of a second-order polynomial, and analytical differentiation, which has been shown to produce results that are insensitive to random errors in the PIV calculation (Fouras and Soria, 1998). Results for an experiment conducted at $Re = 76$ is shown in Fig. 5. The observed Strouhal number was 0.157 ± 0.001, whereas the expected Strouhal number based on the relationship proposed by Williamson (1988a) is 0.152.

The Strouhal number discrepancy is most likely due to non-uniformities in the spanwise direction; either due to oblique shedding patterns [which are known to occur beyond $Re \approx 60$ for a circular cylinder (Williamson, 1988b)], or other irregularities resulting from the mismatched cylinder end-conditions. The vorticity contour plot in Fig. 5 bears a close resemblance to two-dimensional computations obtained at similar Reynolds numbers [such as Braza et al. (1986), Green and Gerrard (1993) and independent computations performed by the authors], validating the PIV measurements.

The true power of this technique is demonstrated in Fig. 6, which shows three-dimensional renderings of the reconstructed surface topography. The overlaid vorticity contours highlight that a strong relationship exists between the measured velocity field (captured on the plane of the submerged laser sheet), and the deformation of the free surface.
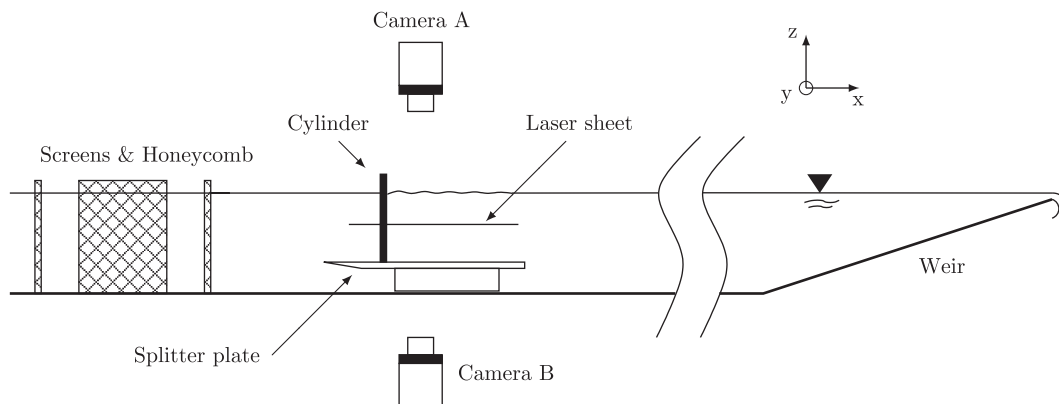

Fig. 4. Schematic diagram showing the setup of the cylinder wake experiments on the water table. The combination of screen, honeycomb and screen was used to reduce free-stream turbulence levels. The splitter plate was used to reduce the size and effect of the bottom wall boundary layer on the two-dimensionality of the flow. Also shown are the cameras and axis co-ordinates.
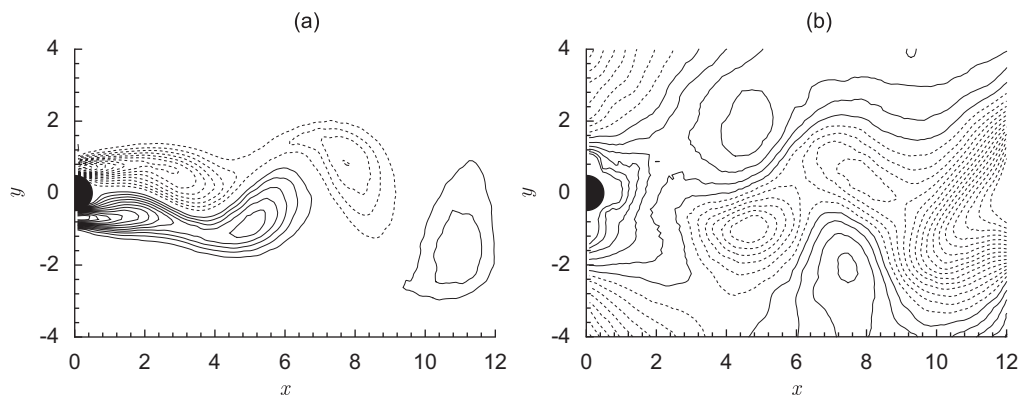

Fig. 5. Plots of (a) vorticity and (b) relative height taken at a Reynolds number $Re = 76$. Solid and dashed lines represent positive and negative values.
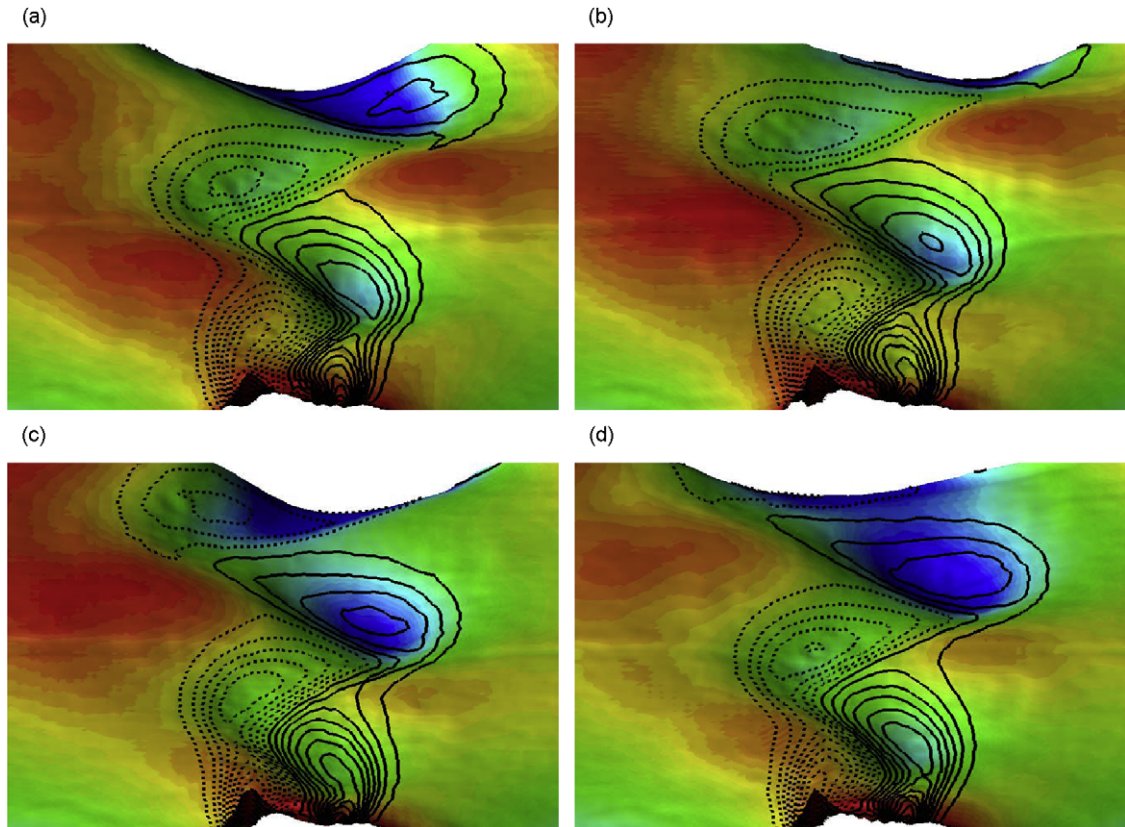
Fig. 6. Three-dimensional iso-surface of calculated surface height overlaid with vorticity contours. Data are shown for Reynolds number Re = 76 for different phases: (a) $t = 0$; (b) $t = T/4$; (c) $t = T/2$; (d) $t = 3T/4$, where T is the shedding period. Solid and dashed lines represent positive and negative values, respectively, of vorticity. The cylinder is located at the bottom of each frame, and flow is from bottom to top. Coloured contours denote surface height, with blue and red corresponding to low and high regions, respectively.

Hydrodynamic theory dictates that the deformation in the surface height relates to the total pressure in the flow, though surface tension and other forces will also contribute to the final topography.

The data also elucidate the high sensitivity of the topography measurements. In the vicinity of the cylinder, the meniscus is clearly visible, with significantly greater relative height than variations measured in the wake. In practice, the meniscus is of the order 1 mm in height. When conducting the experiments, the surface deformation arising from the motion of the wake was invisible to the naked eye. Hence surface deformations an order of magnitude smaller than the scale of the cylinder have been resolved using this technique.

4. Conclusions

A novel technique for the simultaneous measurement of free-surface topography and velocity vector field has been developed. The flow behind a circular cylinder at low Reynolds numbers has been measured using this technique. Both the vorticity field and the Strouhal number closely match the expected results. The free-surface topography, which can be related to the pressure field, exhibits an intimate relationship to the vorticity field. The nature of this relationship is the subject of further investigation.

References

Braza, M., Chassaing, P., Minh, H.H., 1986. Numerical study and physical analysis of the pressure and velocity fields in the near wake of a circular cylinder. Journal of Fluid Mechanics 169, 79–130.

Buchanan, A., Macartney, R., Thompson, M.C., Brocher, E., Hourigan, K., 2007. Hydraulic analogy study of supersonic rectangular jet screech control with cylinders. AIAA Journal 45, 1539–1545.

Fouras, A., Soria, J., 1998. Accurate out-of-plane vorticity calculation from in-plane velocity vector field data. Experiments in Fluids 25, 409–430.

Fouras, A., Hourigan, K., Kawahashi, M., Hirahawa, H., 2006. An improved free surface topographic technique. Journal of Visualization 9, 49–56.

Fouras, A., Dusting, J., Hourigan, K., 2007. A simple calibration technique for stereoscopic particle image velocimetry. Experiments in Fluids 42, 799–810.

Fouras, A., Lo Jacono, D., Hourigan, K., 2008. Target-free stereo PIV: a novel technique with inherent error estimation and improved accuracy. Experiments in Fluids 44, 317–329.

Fu, H., Rockwell, D., 2005. Shallow flow past a cylinder: transition phenomena at low Reynolds number. Journal of Fluid Mechanics 540, 75–97.

Green, R.B., Gerrard, J.H., 1993. Vorticity measurements in the near wake of a circular cylinder. Journal of Fluid Mechanics 246, 657–691.

Raffel, M., Willert, C.E., Kompenhans, J., 1998. Particle Image Velocimetry: A Practical Guide. Springer, Berlin, Germany.

Schenk, O., Gartner, K., 2004. Solving unsymmetric sparse systems of linear equations with PARDISO. Future Generation Computer Systems 20 (3), 475–487.

Tanaka, G., Okamoto, K., Madarame, H., 2000. Experimental investigation on the interaction between a polymer solution jet and a free surface. Experiments in Fluids 29, 178–183.

Williamson, C.H.K., 1988a. Defining a universal and continuous Strouhal-Reynolds number relationship for the laminar vortex shedding of a circular-cylinder. Physics of Fluids 31 (10), 2742–2744.

Williamson, C.H.K., 1988b. Oblique and parallel modes of vortex shedding in the wake of a circular cylinder at low Reynolds numbers. Journal of Fluid Mechanics 206, 579–672.

Williamson, C.H.K., Brown, G.L., 1998. A series in $1/\sqrt{Re}$ to represent the Strouhal–Reynolds number relationship of the cylinder wake. Journal of Fluids and Structures 12 (8), 1073–1085.

Zhang, X., Dabiri, D., Gharib, M., 1994. A novel technique for surface elevation mapping. Physics of Fluids 6, S11.